Materials Advances

ROYAL SOCIETY OF CHEMISTRY

PAPER

View Article Online
View Journal | View Issue

Open Access Article. Published on 07 January 2021. Downloaded on 11/11/2025 6:26:01 PM.
This article is licensed under a Creative Commons Attribution-NonCommercial 3.0 Unported Licence.

Check for updates

Cite this: *Mater. Adv.*, 2021, 2, 793

Ammonia synthesis using Fe/BZY–RuO_2 catalysts and a caesium dihydrogen phosphate-based electrolyte at intermediate temperatures†

Yao Yuan,[a] Shohei Tada[b] and Ryuji Kikuchi*[a]

Received 20th November 2020,
Accepted 29th December 2020

DOI: 10.1039/d0ma00905a

rsc.li/materials-advances

In this study, we developed an Fe_2O_3/BZY (yttrium-doped barium zirconate)–RuO_2 (Fe/BZY–RuO_2) cathode catalyst, which was applied to the electrochemical synthesis of NH_3 using a proton-conducting electrolyte, CsH_2PO_4/SiP_2O_7, at 220 °C and ambient pressure. The highest faradaic efficiency of 7.1% was achieved at −0.4 V (*vs.* open-circuit voltage (OCV)) and the highest NH_3 yield rate of 4.5×10^{-10} mol (s cm^2)$^{-1}$ was achieved at −1.5 V (*vs.* OCV). We also successfully detected N_2H_4 and NH_3 at −0.2 V (*vs.* OCV), which indicated that the N_2 reduction proceeded *via* an associative mechanism. A potentiostatic pulse experiment was conducted under a feed of Ar or N_2 in the cathode at different applied voltages to investigate the N_2 reduction reaction (NRR) mechanism. A model was developed to fit the current response of the potentiostatic pulse experiment, which comprised the decomposition of adsorbed intermediates on the surface of the cathode catalyst, diffusion of H in the cathode catalyst, and an electrical double layer. The results revealed that the rate constant estimated by the model for the decomposition of intermediates, such as NH or N_2H, was lowest at −0.2 V, where N_2H_4 was detected. The fitting results also indicated that the NRR proceeded *via* an associative mechanism at lower applied voltages, while a dissociative mechanism dominated at higher applied voltages.

Introduction

The conventional Haber–Bosch process, which uses iron-based catalysts to produce NH_3, is one of the most important heterogeneous catalytic processes, and is still in use today. It requires high temperatures (400–500 °C) and pressures (50–200 bar), resulting in the consumption of more than 1% of the primary energy supplies of the world and consequently the generation of more than 400 Mt CO_2.[1] Electrochemical N_2 reduction has attracted considerable attention as an alternative because it involves mild reaction conditions and NH_3 is produced directly from N_2 and water using a renewable energy source.[2] However, the greatest challenge is that the production of H_2 from protons at the electrode has priority over NH_3 formation, which leads to a low faradaic efficiency. It is difficult to activate N_2 at low temperatures (<100 °C), while high temperatures (>500 °C) result in the decomposition of the generated NH_3. Thus, an intermediate temperature range (100–500 °C) is preferred for the electrochemical synthesis of NH_3. In addition, at temperatures lower than 200 °C, the total Gibbs energy input per NH_3 production is lower for the above-described direct electrochemical synthesis than that for the combined water electrolysis and Haber–Bosch process system. Consequently, the direct electrochemical synthesis of NH_3 at temperatures <200 °C is an energy-efficient process for the production of NH_3.

Because N_2 is activated by the catalyst, the type of cathode catalyst used determines the efficiency of the direct electrochemical synthesis of NH_3. Ni mesh,[3,4] Pt/C,[5] and Ru/C[5] have been reported as cathode catalysts for use at a temperature of approximately 200 °C. Bicer and Dincer reported the use of a Ni mesh cathode and nano-Fe_2O_3 particles suspended in a molten NaOH–KOH mixture as the electrolyte for an electrolytic cell, which produced NH_3 from N_2 and H_2 at 200 °C[3] at a maximum formation rate of 4.41×10^{-9} mol (s cm^2)$^{-1}$ with a faradaic efficiency of 14.17%.[3] Using a Ru/C cathode and CsH_2PO_4/SiP_2O_7 electrolyte for the synthesis of NH_3 from N_2 and H_2O at 220 °C through solid-state electrolysis, a maximum reaction rate of 1.9×10^{-11} mol (s cm^2)$^{-1}$ and a faradaic efficiency of 0.06% was achieved.[5] Generally, the N_2 reduction reaction (NRR) mechanism can be categorized into two pathways: dissociative and associative. In the dissociative pathway, the NN triple bond is first cleaved to produce N*, while in the associative pathway, H first reacts with N_2 to produce NNH*.[6] If

[a] Department of Chemical System Engineering, The University of Tokyo, 7-3-1, Hongo, Bunkyo-ku, Tokyo 113-8656, Japan
E-mail: rkikuchi@chemsys.t.u-tokyo.ac.jp
[b] Department of Materials Sciences and Engineering, Ibaraki University, Ibaraki 316-8511, Japan

† Electronic supplementary information (ESI) available. See DOI: 10.1039/d0ma00905a

© 2021 The Author(s). Published by the Royal Society of Chemistry

Open Access Article. Published on 07 January 2021. Downloaded on 11/11/2025 6:26:01 PM.
This article is licensed under a Creative Commons Attribution-NonCommercial 3.0 Unported Licence.

the N–N bond is retained during the addition of H, N_2H_4 will be produced. As suggested by DFT calculation results, the associative mechanism is usually the most favourable pathway for the electrochemical synthesis of NH_3.[7,8] However, most experimental studies do not report the formation of N_2H_4,[9–13] with the exception of the study conducted by Bao *et al.*[14] This might be because N–N bond dissociation occurs rapidly in intermediates such as NNH_2* to produce NH_3, owing to the large free energy change that occurs over widely used precious metal cathode catalysts. Consequently, the apparent production rate of N_2H_4 was negligible. Singh *et al.* reported that for low N_2 binding energies on transition metal surfaces, thermochemical N–N bond dissociation has a lower activation barrier than that of the associative NRR in the electrochemical pathway.[17] This was established using calculations by assuming an appropriate N–N transition-state scaling. These results might also explain the lack of N_2H_4 detection.

In this study, a novel iron-based composite, a reduced α-Fe_2O_3/BZY (yttrium-doped barium zirconate), was used as a cathode catalyst for the electrolytic synthesis of NH_3 from N_2 and H_2 at 220 °C in a double-chamber cell. The reduced α-Fe_2O_3/BZY (Fe/BZY) catalyst was also combined with RuO_2 and tested as a cathode catalyst for the electrolytic synthesis of NH_3 from N_2 and water vapor at 220 °C in a double-chamber cell. Fe/BZY exhibits electrical conductivity and should possess proton conductivity and catalytic activity for N_2 reduction; these are the desired properties for a cathode catalyst applied in the electrolytic synthesis of NH_3 (Table S1, ESI†). A Pt anode and CsH_2PO_4/SiP_2O_7 electrolyte[15] were used for the electrochemical synthesis of NH_3 at 220 °C and atmospheric pressure. There are three requirements for the electrocatalytic NRR to achieve a high activity and selectivity towards NH_3: (i) the catalysts should bind strongly to N_2, (ii) a large reduction potential should be applied at which the NRR mechanism is in its irreversible limit,[16] and (iii) a nonaqueous electrolyte, with a lowered proton donor activity that limits the proton availability at the electrode surface and consequently improves the selectivity towards NH_3, should be used.[17,18] The electrode catalysts and electrolyte employed in this study meets these requirements. To elucidate the NRR pathway over the electrode catalysts developed in this study, the intermediates on the cathode catalyst surface were analyzed by potentiostatic pulse experiments under dry N_2 or Ar atmosphere by applying a variety of voltages. To interpret the current response of the potentiostatic experiments, a model comprising adsorbed intermediate decomposition, H diffusion in the catalyst, and an electrical double layer was developed.

Experimental

Preparation of reduced α-Fe_2O_3/BZY[19]

The yttrium-doped barium zirconate ($BaZr_{0.8}Y_{0.2}O_{3-\sigma}$) powder was prepared by a conventional solid-state reaction. The reagents used were $BaCO_3$ (98% purity, Wako Pure Chemical Industries Ltd, Osaka, Japan), Y_2O_3 (99.9% purity, Wako Pure Chemical Industries Ltd, Osaka, Japan), and ZrO_2 (98% purity, Wako Pure Chemical Industries Ltd, Osaka, Japan). The materials were mixed in stoichiometric quantities and ball milled in ethanol overnight. After drying, the precursor was calcined at 1400 °C for 12 h to yield the BZY powder. The BZY powder and α-Fe_2O_3 (20–40 nm, Wako Pure Chemical Industries Ltd, Tokyo, Japan) were mixed in a weight ratio of 1 : 4 and ball milled in ethanol overnight. After drying, the mixture was sintered at 1300 °C for 12 h to form an α-Fe_2O_3/BZY composite. The resultant α-Fe_2O_3/BZY composite was reduced in H_2 atmosphere at 500 °C for 1 h and cooled to 25 °C under N_2.

Preparation of the reduced α-Fe_2O_3/BZY and RuO_2 mixtures

The reduced α-Fe_2O_3/BZY was mixed with RuO_2 (Practical Grade, Wako Pure Chemical Industries Ltd, Osaka, Japan) and ground to fabricate the cathode materials.

Preparation of CsH_2PO_4/SiP_2O_7[5]

CsH_2PO_4 was prepared using Cs_2CO_3 (Wako 1st Grade, Wako Pure Chemical Industries Ltd, Osaka, Japan) and H_3PO_4 (85 wt% in water, Sigma-Aldrich Co. LLC, Missouri, USA) in stoichiometric quantities. After dissolution in distilled water, the precursor was dried at 120 °C overnight. SiP_2O_7 was prepared from SiO_2 (99.9% purity, Wako Pure Chemical Industries Ltd, Osaka, Japan) and H_3PO_4 as follows: SiO_2 and H_3PO_4 were mixed in a molar ratio of 1 : 2.5, and heated at 200 °C for 3 h. After drying at 100 °C for 24 h, the precursor was ground into a powder and heated at 122 °C for 24 h. Finally, the powder was calcined at 700 °C for 3 h to attain the SiP_2O_7 phase. Subsequently, the prepared CsH_2PO_4 and SiP_2O_7 were mixed in a molar ratio of 1 : 1 and ground to form the CsH_2PO_4/SiP_2O_7 composite.

Preparation of electrolysis cells

The CsH_2PO_4/SiP_2O_7 powder was pressed into a ∅ 20 mm disk. The reduced α-Fe_2O_3/BZY (0.075 g) and RuO_2 (0.075 g) powders were mixed and loaded on the cathode side of the CsH_2PO_4/SiP_2O_7 disk and pressed at a pressure of 20 MPa for 10 min. Porous carbon paper (∅ 10 mm, TGP-H-120, Toray Industries, Inc., Tokyo, Japan) was used as the current collector on the cathode side. A Pt/C loaded carbon paper of ∅ 10 mm (Pt loading of 1 mg cm^{-2}, Miclab, Kanagawa, Japan) was used as the anode catalyst. Pt wires connected to the Pt mesh or Pt/C were used as the terminal on the anode side, while the Pt wires connected to the carbon paper acted as the terminal on the cathode side. Polytetrafluoroethylene (PTFE) sheet (Gore Hyper-Sheet Gasket, W. L. Gore & Associate, Inc., Delaware, USA) layers with an appropriate thickness were used as the gas seal. The two-chamber reactor setup is illustrated in Fig. 1.

Characterization

X-ray diffraction was performed at 100 kV and 40 mA in the 2θ range of 20–80° (XRD, Rigaku RINT 2400). The cross-sectional morphologies of the electrolysis cells were observed by scanning electron microscopy (SEM, Hitachi S-4700, Tokyo, Japan) and energy dispersive X-ray spectroscopy (EDX, Super Xerophy, Horiba, Kyoto, Japan). Temperature-programmed reduction (TPR) experiments were performed in a flow system (Quantachrome,

 © 2021 The Author(s). Published by the Royal Society of Chemistry

Open Access Article. Published on 07 January 2021. Downloaded on 11/11/2025 6:26:01 PM.
This article is licensed under a Creative Commons Attribution-NonCommercial 3.0 Unported Licence.

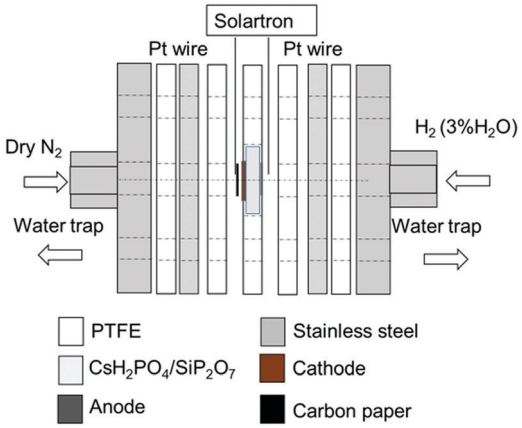

Fig. 1 Experimental setup for electrochemical synthesis of NH_3.

CHEMBET-3000, Florida, USA). To confirm that the addition of the Ru species could suppress the oxidation of Fe, the samples were pretreated at 220 °C for 30 min in Ar at a flow rate of 50 mL min^{-1} and heating rate of 10 °C min^{-1} and cooled to room temperature. After flushing with diluted H_2 (5% H_2 in Ar) at a flow rate of 50 mL min^{-1} for 1 h, the samples were heated to 220 °C at a heating rate of 10 °C min^{-1} and reduced for 1 h. After flushing with Ar at a flow rate of 50 mL min^{-1} for 30 min, the samples were oxidised in diluted O_2 (5% O_2 in He) at a flow rate of 50 mL min^{-1} for 30 min and cooled to room temperature in Ar. The samples were again flushed with diluted H_2 and heated to 1000 °C. The proton conductivity of the cell was evaluated by alternating current impedance measurements from 1 MHz to 0.05 Hz, with an AC amplitude of 20 mV under 3%-humidified H_2 (or 20%-humidified Ar) on the anode side and dry N_2 on the cathode side (Solartron 1260, Solartron Instruments, Hampshire, UK). Humidified H_2 (3% H_2O) and Ar (20% H_2O) were obtained by bubbling H_2 or Ar gas into distilled water in a water bath at room temperature and at 60 °C, respectively. The potentiostatic pulse experiment,[20,21] was conducted by applying bias voltages for 400 s and then stepping to an open circuit voltage (OCV) (SP 300, Bio-Logic, Seyssinet-Pariset, France).

Pretreatment of the cell

The cell was heated from 25 °C to 220 °C at a heating rate of 2.8 °C min^{-1}, with a gas flow of dry N_2 on the cathode side and dry Ar on the anode side from 25 °C to 120 °C. From 120 °C to 220 °C, humidified H_2 gas was fed to the anode. In the steady state, a voltage of −2 V (*vs.* OCV) was applied to the cell for 1 h to reduce RuO_2.

Blank experiments using open circuit conditions and testing

The following three blank experiments were conducted at 220 °C at OCV conditions before performing the reaction tests. Blank experiment 1 was conducted using a gas flow of 3%-humidified H_2 on the anode side and dry N_2 on the cathode side. Blank experiment 2 was performed with a gas flow of 20%-humidified Ar on the anode side and dry Ar on the cathode side. Blank experiment 3 was conducted with a gas flow of 20%-humidified Ar on the anode side and dry N_2 on the cathode side. Electrolysis was performed under the same conditions as blank experiment 1. A direct current voltage *vs.* OCV was applied between the anode and cathode under potentiostatic conditions. The total gas flow rate was kept constant at 25 mL (STP) min^{-1} on both sides. The outlet gases were trapped in a distilled water trap for 30 min. The amount of NH_3 and hydrazine in the distilled water trap was quantified by the salicylate method and Watt and Chrisp's method,[22] respectively, using a colorimeter (DR900, Hach Company). The reagents used were salicylate and cyanurate reagents (Nitrogen–Ammonia Reagent Set, Salicylate Method, 10 mL, Hach Company) for NH_3 quantification and hydrazine reagent (HydraVer® 2 Hydrazine Reagent, Hach Company) for the quantification of hydrazine.

Results and discussion

Characteristics

Fig. 2 shows the XRD patterns of the α-Fe_2O_3, BZY, and Fe_2O_3/BZY composites. Fig. 2(a) shows the XRD pattern of the as-obtained α-Fe_2O_3. In Fig. 2(b), all the peaks could be assigned to those of a typical perovskite structure, suggesting that BZY was

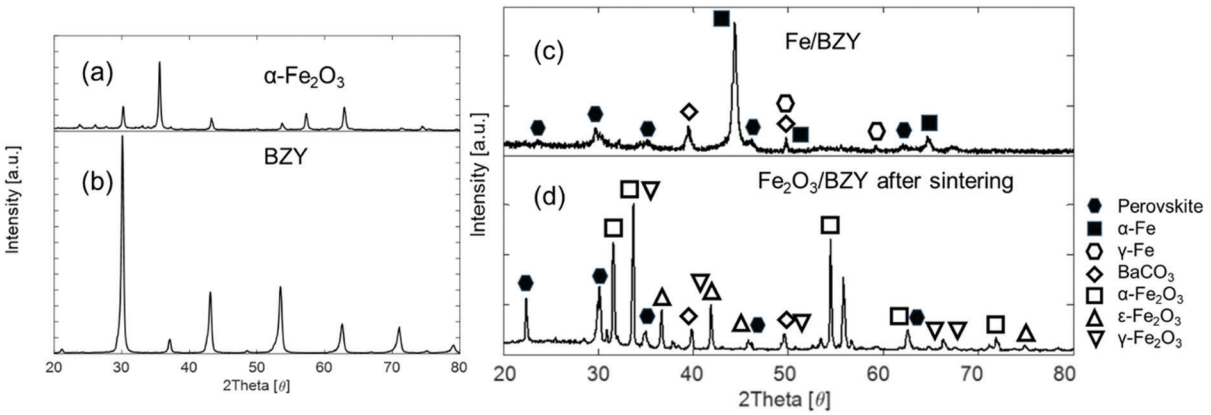

Fig. 2 XRD patterns of (a) as-obtained α-Fe_2O_3, (b) as-calcined BZY powders, (c) Fe_2O_3/BZY reduced at 500 °C for 1 h, and (d) as-synthesized Fe_2O_3/BZY at a weight ratio of 4 : 1 and calcined at 1300 °C for 12 h in air.

Open Access Article. Published on 07 January 2021. Downloaded on 11/11/2025 6:26:01 PM.
This article is licensed under a Creative Commons Attribution-NonCommercial 3.0 Unported Licence.

successfully synthesised. According to Fig. 2(c), after the mixture of BZY powder and α-Fe_2O_3 was sintered at 1300 °C, some of the BZY was decomposed into carbonates and oxides, and the phase transition of α-Fe_2O_3 to ε-Fe_2O_3 and γ-Fe_2O_3 occurred simultaneously. The iron oxides were reduced to a metallic state, as shown in Fig. 2(d). In contrast, the perovskite structure in the composite remained stable after the reduction treatment.

Fig. 3 shows the SEM-EDS cross-sectional images of the electrolysis cells containing the Fe_2O_3/BZY–RuO_2 cathode catalyst. It is evident from Fig. 3(a) and (b) that the cathode catalyst layer reduced in size after the electrolysis reaction, which probably resulted from the reduction of RuO_2. In addition, it is clear that the particle size of the cathode catalyst increased after electrolysis. The particle size increase is also supported by the EDS mapping images of the Ru species (Fig. 3(c) and (d)), which indicates that a slight aggregation of the Ru species occurred during the pre-reduction treatment and electrolysis reaction. The aggregation might have been caused by the reduction of RuO_2 and the NRR on the active sites. Nevertheless, even after the electrolysis reaction, the Ru species were uniformly dispersed over Fe/BZY, as indicated in the magnified SEM-EDS image (Fig. 3(e)). There seems to be no clear interpenetration of the electrolyte material into the cathode catalyst layer after electrolysis because the distribution of P, Si, and Cs is confined to the electrolyte phase before and after the electrolysis test, as shown in Fig. 3(c) and (d). This implies that no reaction occurred between the acidic electrolyte material and cathode catalyst. In some fuel cells where caesium phosphate-based electrolytes are used, the electrolyte materials penetrate the electrode layers after current loading.[23] This is because the wettability of the electrolyte materials towards the electrocatalyst materials is low, and accordingly the electrolyte materials are retained within the electrolyte layer.

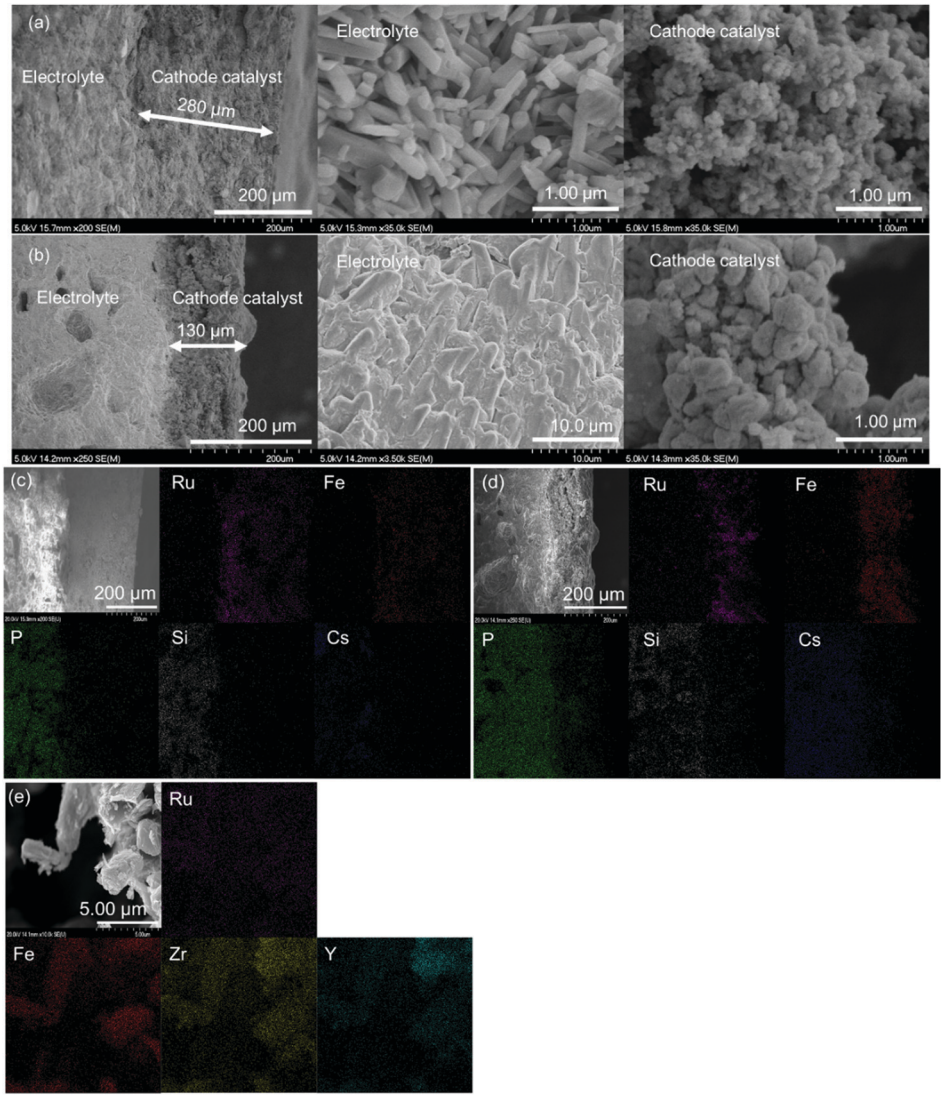

Fig. 3 Cross sectional SEM-EDS images of the electrolysis cells containing a cathode catalyst which consists of a mixture of 75 mg Fe/BZY and 75 mg RuO_2: (a) as-prepared before H_2 reduction, but prior to electrocatalytic tests, (b) after electrocatalytic tests, (c) as-prepared before H_2 reduction, but prior to electrocatalytic tests, (d) after electrocatalytic tests, and (e) magnified image after electrocatalytic tests.

 © 2021 The Author(s). Published by the Royal Society of Chemistry

Open Access Article. Published on 07 January 2021. Downloaded on 11/11/2025 6:26:01 PM.
This article is licensed under a Creative Commons Attribution-NonCommercial 3.0 Unported Licence.

The reducibility of Fe/BZY and Fe/BZY–RuO_2 was investigated by TPR (Fig. 4). In the TPR profile, a sharp peak appears at low temperatures and a broad peak appears at high temperatures. The low temperature peak exists only in the profile of the RuO_2-containing catalysts, whereas the high temperature peak is observed in the Fe/BZY-containing catalysts. Accordingly, the low- and high-temperature peaks are attributed to the reduction of the RuO_2 and iron oxide species, respectively. The low temperature peaks, indicated by ① and ② in the TPR profiles, correspond to the reduction of the RuO_2 oxidised by the dilute O_2/He gas at 220 °C. The reduction temperatures of RuO_2 in Fig. 4 are lower than those shown in Fig. S1 (ESI†), which implies that fresh RuO_2 is more easily reduced. The TPR profile of Fe/BZY shown in Fig. S1 (ESI†) indicates that the iron component in the prepared Fe/BZY was partially oxidised in ambient atmosphere. The high temperature peaks, indicated by ③ and ④ in the TPR profile, can most likely be assigned to the reduction of Fe_2O_3 to Fe_3O_4. The peaks indicated by ⑤ and ⑥ are derived from the reduction of Fe_3O_4 to Fe.[24] Only in the TPR profile of Fe/BZY–RuO_2 (red) in Fig. 4 is a new peak (⑦) observed at 186 °C. This peak could stem from the reduction of the fresh Fe_2O_3 formed on the surface of Fe in dilute O_2/He gas at 220 °C. It follows that with the addition of RuO_2 (the RuO_2 is partially reduced by H_2 generated at the cathode), the *in situ* oxidised Fe, which most likely forms by the steam present under the electrolysis conditions, could be reduced at 220 °C, and thus the activity of the Fe/BZY catalyst could be regained.

Blank experiments at OCV

An error in quantification might occur if NH_3 from the ambient atmosphere adsorbs on the cell or NH_3 is absorbed by the water trap. Accordingly, three kinds of blank experiments were conducted under open-circuit conditions. Blank experiments 1 and 2 were intended to exclude the possibility of ambient NH_3 absorption in the water trap. Blank experiment 3 aimed to examine whether the gas leakage between the anode and cathode chambers could cause catalytic NH_3 production in the H_2 and N_2 gas flows to the anode and cathode, respectively. The amount of trapped NH_3 during the blank experiments, which included a collection time of 30 min, was below the detection limit (0.01 mg-N L^{-1}, equivalent to 2.5×10^{-11} mol (s $cm^2)^{-1}$). Therefore, both the ambient and catalytically generated NH_3 could be ignored. Furthermore, N_2H_4 could not be detected in the blank experiments, which suggests that the colorimetric error due to other factors could be ignored (1 μg N_2H_4 L^{-1} is equivalent to 1.1×10^{-12} mol (s $cm^2)^{-1}$) (Table S1, ESI†). Since the reagents used to synthesize the catalyst and electrolyte did not contain any N species, the origin of NH_3 could be confirmed to be from the reaction of the feeding N_2 gas flow.

Electrolysis results

The electrolysis cell was polarized under the flow of dry N_2 to the cathode and humidified H_2 to the anode, and the effluent gas from the electrode chambers was passed through a water trap for gas collection and analysis. Fig. 5 summarises the gas analysis results for the voltages applied (*vs.* OCV). Both NH_3 and N_2H_4 were detected in the applied voltage range from −0.1 V to −2.5 V. Because the products were only detected in the water trap of the cathode side, the cross leakage between the anode and cathode could be neglected. The detection of N_2H_4 suggests that N_2 reduction proceeded *via* the association mechanism.[7,25] Notably, the NH_3 production rate when using only RuO_2 (Fig. S6, ESI†) or Fe/BZY (Fig. S7, ESI†) as the cathode catalyst was approximately 1×10^{-10} mol (s $cm^2)^{-1}$; no N_2H_4 was detected. The nitrogen reduction rate over the RuO_2 cathode reduced prior to electrolysis, at low applied voltages, was comparable to that over the Fe/BZY–RuO_2 catalyst. Despite the similar nitrogen reduction rates at low applied voltages, no N_2H_4 was detected over the RuO_2 catalyst, which supports the theory that the N–N bond dissociation in the intermediates is fast over precious metal catalysts during the associative mechanism.[17] Another possibility is that the NRR proceeds

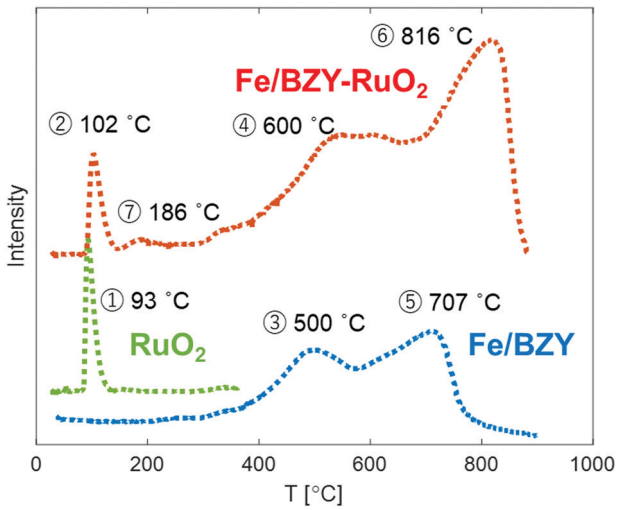

Fig. 4 TPR profiles of 5 mg RuO_2 (green), 5 mg Fe/BZY (blue), 5 mg RuO_2, and 5 mg of the Fe/BZY mixture (red) oxidized at 220 °C.

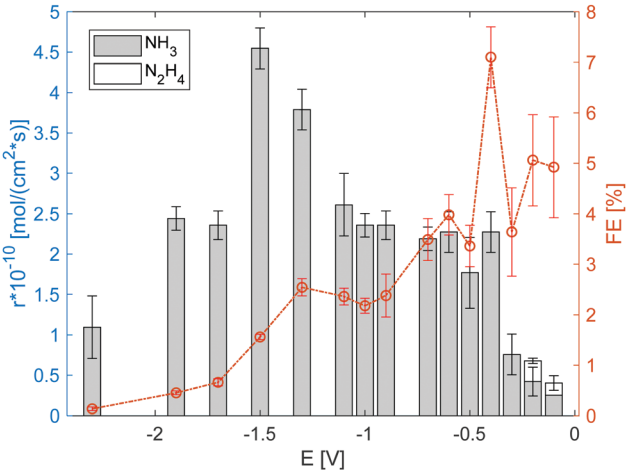

Fig. 5 Production rate and corresponding faradaic efficiency (FE) of NH_3 and N_2H_4 under 3% humidified H_2 anode atmosphere. The error bars are standard deviations.

Open Access Article. Published on 07 January 2021. Downloaded on 11/11/2025 6:26:01 PM.
This article is licensed under a Creative Commons Attribution-NonCommercial 3.0 Unported Licence.

via the dissociation mechanism when only the RuO_2 catalyst is used. When the applied voltage was higher, the faradaic efficiency decreased to 0.5%, which indicates that the RuO_2 electrode surface was mainly occupied by H_2 species and H_2 evolution was prominent. Over the Fe/BZY catalyst, a similar nitrogen reduction rate was attained, but the faradaic efficiency was quite low (less than 1%). As indicated by the TPR spectrum in Fig. 4, the Fe surface of the Fe/BZY electrode catalyst could be partially oxidised. Because iron oxides are rather inactive in the NRR,[9] such partially oxidised Fe surfaces function as H_2 generation sites, leading to a small faradaic efficiency over the Fe/BZY catalyst.

Fig. 6 shows the impedance spectrum measured under dry N_2 in the cathode and humidified H_2 in the anode, as represented in the Nyquist plot. Fig. 7(a) shows the equivalent circuit model used to fit the impedance spectra. In the equivalent circuit, one ohmic resistance (R_s) and two parallel circuits of a constant phase element (CPE) and resistance (R_1, R_2) are included to express the electrode reaction processes, along with an inductor (L_1). The inductance is attributed to the inductance of the cables used in the impedance measurement apparatus, and thus was invariant to measurement conditions (Table S3, ESI†). Fig. 7(b) summarizes R_s, R_1, and R_2 at different bias potentials. R_s is mainly attributable to the ohmic resistance of the electrolyte, whereas R_1 and R_2 are attributed to non-ohmic polarisation resistance. The ohmic resistance is constant irrespective of the applied voltage, and the non-ohmic polarisation resistance decreases from −0.1 V to −0.5 V. The characteristic frequency of the arc for R_2 (f_2 in Table S3, ESI†) is less than 10 Hz at the applied voltages, and consequently, the process characterized by the arc of R_2 in the RC parallel circuit can be assigned to a slow process, such as gas diffusion in the electrode.[26] In addition, the characteristic frequency of the high-frequency arc is in the order of kHz. Accordingly, it is feasible that the process characterized by the high-frequency arc of R_1 is related to electrochemical reactions at the electrode surface and electrode/electrolyte interface. Notably, the smallest non-ohmic polarisation resistance at −0.4 V corresponds to the highest faradaic efficiency at −0.4 V, as shown in Fig. 5.

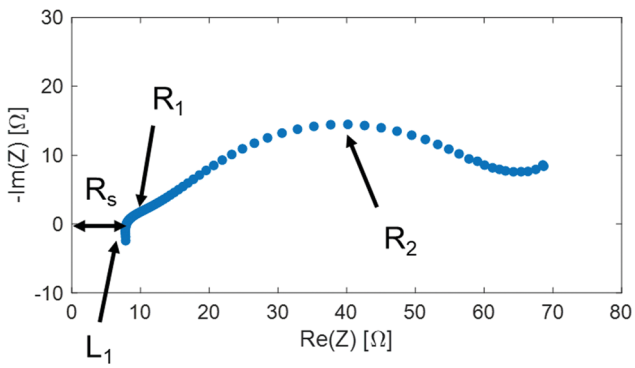

Fig. 6 Impedance under dry N_2 cathode atmosphere and 3%-humidified H_2 anode atmosphere.

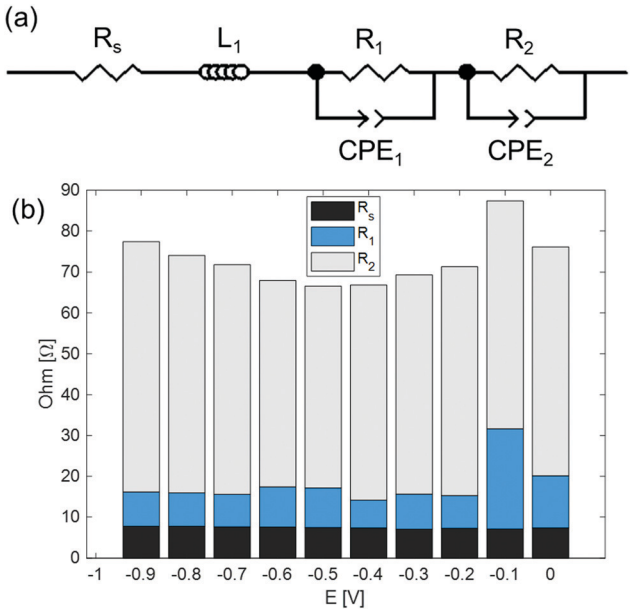

Fig. 7 (a) Simplified equivalent circuit model. (b) R_s, R_1, and R_2 parameters obtained from the equivalent circuit fitting results.

Model of potentiostatic pulse experiment

Fig. 8 illustrates the potential step program and current response during the potentiostatic pulse experiment. In this experiment, first, a constant current of i_w is loaded at an applied voltage of E_w for the period t_w. Consequently, the applied voltage is quickly converted stepwise to the OCV. Upon the quick return of the applied voltage to the OCV, the current starts to flow contrarily to i_w and gradually ceases to 0. Here, the reverse current is denoted as i_{ocv}, and the period for i_{ocv} to reach 0 is t_{ocv}. In the following experiments, E_w was applied for the period t_w = 400 s.

The potentiostatic pulse experiments were conducted by feeding humidified H_2 to the anode and dry N_2 or dry Ar to the cathode. The former condition is similar to the electrolysis mode used for the synthesis of NH_3; in the latter, the same gas atmosphere is used at the cathode side as in proton pumping. During the period t_w, protons are transferred from the anode to cathode and electrons are received to form a H layer (H_{ads1}) at the electrolyte/cathode interface. Subsequently, the adsorbed H_{ads1} atoms dissolve into the cathode, where they are in equilibrium with the H_{metal} concentration just below the cathode/electrolyte interface (H_{metal} denotes H atoms in the bulk metal of the cathode catalyst). This is followed by the diffusion and trapping of the H_{metal} atoms in the bulk metal.[27] The H_{metal} atoms then cross the cathode to the cathode/gas interface and reach an equilibrium value (H_{ads2}) on the cathode surface. When dry Ar feed is used in the cathode, only H_{ads2} is assumed to reside at the surface of the electrode catalyst during the period t_w, while under a dry N_2 feed, N_2-containing species (N_2H_{ads2} and/or NH_{ads2}) could adsorb on the electrode catalyst surface in addition to H_{ads2}. In this model, i_{ocv} is derived from three types of reactions. The first reaction involves the decomposition and ionisation of adsorbed species on the surface of the cathode

 © 2021 The Author(s). Published by the Royal Society of Chemistry

Open Access Article. Published on 07 January 2021. Downloaded on 11/11/2025 6:26:01 PM.
This article is licensed under a Creative Commons Attribution-NonCommercial 3.0 Unported Licence.

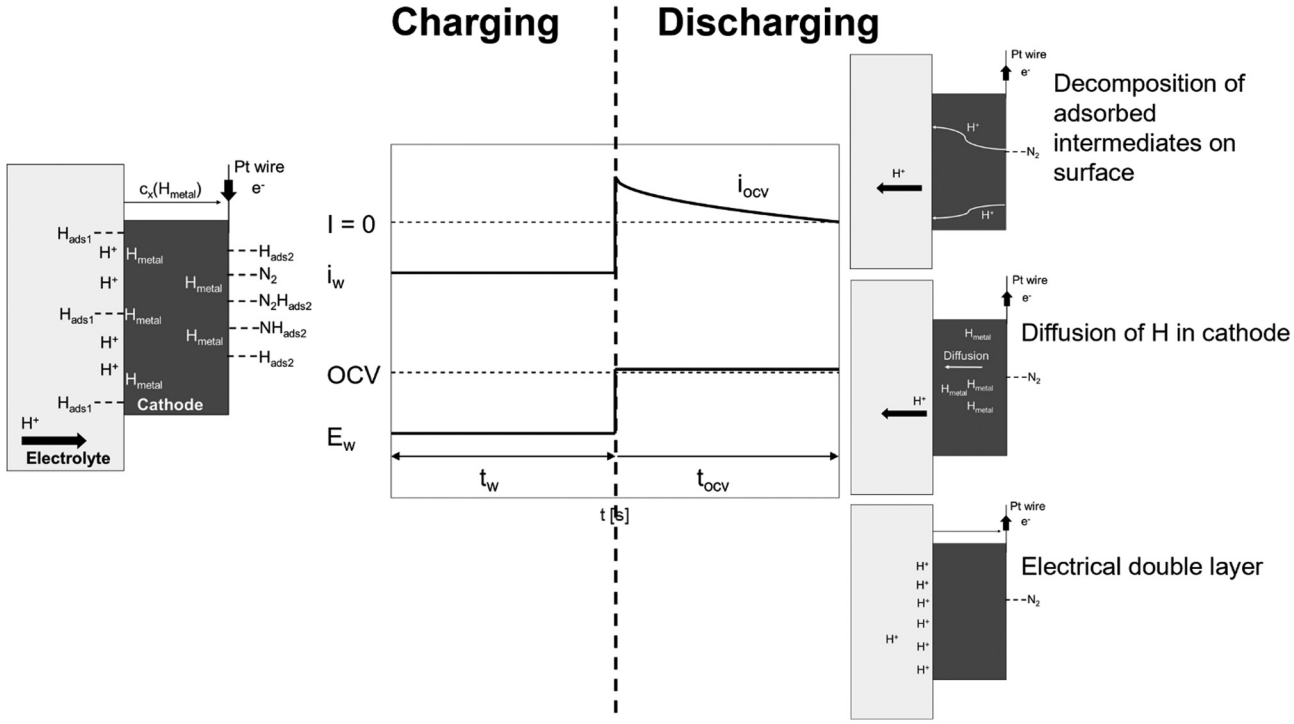

Fig. 8 Schematic diagram of potential step and current response during potentiostatic pulse experiment and general model profiles of charging (t_w) and discharging (t_{ocv}) processes under dry N_2.

catalyst. When using a dry Ar feed, only the $H_{ads2} \rightarrow H^+ + e^-$ reaction needs to be considered as the reverse current source during t_{ocv}. When using a dry N_2 feed, the decomposition reactions of the intermediates, such as N_2H_{ads2} and/or NH_{ads2}, should also be considered. The second reaction stems from the remaining H_{metal} in the bulk metal, while the third reaction is due to the electrical double layer.

The i_{ocv} from the remaining H_{metal} in the bulk metal will be discussed first, based on the following analyses. According to Pound *et al.*,[28,29] when the proton transfer across the cathode/electrolyte interface is very fast, the i_{ocv} from $H_{metal} \rightarrow H^+ + e^-$ is only controlled by the diffusion of H_{metal}. They adopted the following boundary conditions at the electrode surface as

$$\begin{cases} c(0,t) = 1 \\ \dfrac{\partial c}{\partial x}(x,0) = 0 \\ c \rightarrow 0 \text{ as } x \rightarrow \infty \end{cases}$$

where x is the distance from the electrolyte/cathode interface, t is the diffusion time and c stands for the consentration,[26] because H_{metal} cannot diffuse to the electrode/gas boundary within a charge time of less than 20 seconds, which they applied to the analysis of their experimental results.[29] In this work, we adopted a long enough charging time of 400 seconds, and accordingly H_{metal} atoms are considered to diffuse to the cathode/gas interface to form the adsorbed hydrogen on the cathode surface, and are released as gaseous H_2 in a steady state. Therefore, the boundary conditions are different from those by Pound *et al.*, and with appropriate boundary conditions in our study it is feasible to take into account the contributions of the decomposition of the adsorbed species at the cathode surface and the electrical double layer at the cathode/electrolyte interface to the i_{ocv}.

At the charging step, it can be assumed that the H atom traps are unsaturated, and therefore the trapping rate constant, k, remains constant. Fick's second law of diffusion can be modified with kc, where k is the trapping rate constant and $c(x,t)$ is the concentration of H_{metal} at a distance x from the electrolyte/cathode interface and at a time t, which starts from $t_w = 0$. D is the diffusion coefficient of H_{metal} in the cathode.

$$D\frac{d^2c}{dx^2} = kc, \tag{1}$$

$$c = Ae^{\sqrt{k/D}x} + Be^{-\sqrt{k/D}x}. \tag{2}$$

θ in eqn (3) represents the adsorbed H on the electrolyte side at the interface of the cathode and electrolyte. The boundary conditions thus become:

$$\begin{cases} D\dfrac{dc}{dx}(0) = k_{ex}c(0) - k_{in}\theta \\ D\dfrac{dc}{dx}(X) = -k^{ex}c(X), \end{cases} \tag{3}$$

where k_{ex} and k_{in} are the rate constants of H moving out of the cathode and the ingress of H into the cathode at the electrolyte/cathode interface, respectively. X represents the thickness of the cathode catalyst, and has a value of 200 μm, as shown in Fig. 3(a) and (b). By substituting eqn (2) into eqn (3), the

Open Access Article. Published on 07 January 2021. Downloaded on 11/11/2025 6:26:01 PM.
This article is licensed under a Creative Commons Attribution-NonCommercial 3.0 Unported Licence.

following is obtained:

$$\begin{cases} \sqrt{kD}(A-B) = k_{\mathrm{ex}}(A+B) - k_{\mathrm{in}}\theta \\ \sqrt{kD}\left(A\mathrm{e}^{\sqrt{k/D}X} - B\mathrm{e}^{-\sqrt{k/D}X}\right) = -k^{\mathrm{ex}}\left(A\mathrm{e}^{\sqrt{k/D}X} + B\mathrm{e}^{-\sqrt{k/D}X}\right) \end{cases}. \tag{4}$$

Thus, A and B can be obtained by eqn (5) and (6).

$$B\mathrm{e}^{-\sqrt{k/D}X} = \frac{\sqrt{kD}+k^{\mathrm{ex}}}{\sqrt{kD}-k^{\mathrm{ex}}}A\mathrm{e}^{\sqrt{k/D}X}, \tag{5}$$

$$k_{\mathrm{in}}\theta = \left(\left(k_{\mathrm{ex}} - \sqrt{kD}\right) + \left(k_{\mathrm{ex}} + \sqrt{kD}\right)\frac{\sqrt{kD}+k^{\mathrm{ex}}}{\sqrt{kD}-k^{\mathrm{ex}}}\mathrm{e}^{2\sqrt{k/D}X}\right)A. \tag{6}$$

In the discharging step, taking into account the effect of the H_{metal} atoms trapped in the bulk metal, Fick's second law of diffusion can be modified with kc; time t starts from $t_{\mathrm{ocv}} = 0$.

$$\frac{\partial c}{\partial t} - D\frac{\partial^2 c}{\partial x^2} = -kc. \tag{7}$$

The boundary conditions thus become:

$$\begin{cases} c(0,t) = 0 \\ \frac{\partial c}{\partial x}(X,t) = 0 \end{cases}. \tag{8}$$

The following assumption is then made:

$$\begin{cases} c(x,t) = f(x)g(t) \\ D\frac{\mathrm{d}^2 f}{\mathrm{d}x^2} = k_{\mathrm{f}} f \end{cases}, \tag{9}$$

where, if $k_{\mathrm{f}} > 0$, then $f = a\mathrm{e}^{\sqrt{k_{\mathrm{f}}/D}x} + b\mathrm{e}^{-\sqrt{k_{\mathrm{f}}/D}x}$. By substituting the boundary conditions, $f = 0$ can be obtained. If there is no H trapping, which implies $k = 0$, then $f = 0$. If $k_{\mathrm{f}} < 0$, then $f = a_{k_{\mathrm{f}}}\cos\sqrt{-k_{\mathrm{f}}/D}x + b_{k_{\mathrm{f}}}\sin\sqrt{-k_{\mathrm{f}}/D}x$. By substituting the boundary conditions, $a_{k_{\mathrm{f}}} = 0$ and $b_{k_{\mathrm{f}}} \neq 0 \Rightarrow \sqrt{-k_{\mathrm{f}}/D}X = \left(n+\frac{1}{2}\right)\pi$, where n is an integer. Because $k_{\mathrm{g}} = k_{\mathrm{f}} - k < 0$, $\frac{\mathrm{d}g}{\mathrm{d}t} = k_{\mathrm{g}}g \Rightarrow g = c_{k_{\mathrm{g}}}\mathrm{e}^{k_{\mathrm{g}}t}$. F is Faraday's constant. Thus, the following is obtained:

$$c(x,t) = \sum_n A_n \sin\left(n+\frac{1}{2}\right)\pi\frac{x}{X}\mathrm{e}^{-\left(((n+1/2)\pi/X)^2 D + k\right)t}, \tag{10}$$

$$\begin{aligned} i &= FD\frac{\mathrm{d}c}{\mathrm{d}x}(0,t) \\ &= \pi FD\sum_n \left(n+\frac{1}{2}\right)\frac{A_n}{X}\mathrm{e}^{-\left(((n+1/2)\pi/X)^2 D + k\right)t}. \end{aligned} \tag{11}$$

By substituting eqn (2) into eqn (10), the initial discharging condition is obtained as:

$$A\mathrm{e}^{\sqrt{k/D}x} + B\mathrm{e}^{-\sqrt{k/D}x} = \sum_n A_n \sin\left(n+\frac{1}{2}\right)\pi\frac{x}{X}. \tag{12}$$

Taking integrals on both sides of eqn (12), we obtain eqn (13):

$$\begin{aligned} &\int_0^X \sin\left(n+\frac{1}{2}\right)\pi\frac{x}{X}\left(A\mathrm{e}^{\sqrt{k/D}x} + B\mathrm{e}^{-\sqrt{k/D}x}\right)\mathrm{d}x \\ &= A_n\int_0^X \sin^2\left(n+\frac{1}{2}\right)\pi\frac{x}{X}\mathrm{d}x. \end{aligned} \tag{13}$$

Assuming $p = \sqrt{k/D}$ and $q = \left(n+\frac{1}{2}\right)\frac{\pi}{X}$, we obtain eqn (14) and (15),

$$\begin{cases} A_n\int_0^X \sin^2\left(n+\frac{1}{2}\right)\pi\frac{x}{X}\mathrm{d}x = \frac{A_n X}{2} \\ \int_0^X \sin\left(n+\frac{1}{2}\right)\pi\frac{x}{X}(A\mathrm{e}^{px} + B\mathrm{e}^{-px})\mathrm{d}x \\ \quad = \frac{(-1)^n p(A\mathrm{e}^{pX} - B\mathrm{e}^{-pX}) + q(A+B)}{p^2+q^2}, \end{cases} \tag{14}$$

$$A_n = \frac{2}{X}\frac{(-1)^n p(A\mathrm{e}^{pX} - B\mathrm{e}^{-pX}) + q(A+B)}{p^2+q^2}. \tag{15}$$

Thus, i_{ocv} derived from H_{metal} is given as:

$$\begin{aligned} i(t) &= \pi FD\sum_n \left(n+\frac{1}{2}\right)\frac{A_n}{X}\mathrm{e}^{-\left(((n+1/2)\pi/X)^2 D + k\right)t} \\ &= \frac{\pi FD}{X^2}\sum_n (2n+1) \\ &\quad \times \frac{(-1)^n\sqrt{k/D}\left(A\mathrm{e}^{\sqrt{k/D}X} - B\mathrm{e}^{-\sqrt{k/D}X}\right) + \left(n+\frac{1}{2}\right)\frac{\pi}{X}(A+B)}{\left(\frac{k}{D} + \left(\left(n+\frac{1}{2}\right)\frac{\pi}{X}\right)^2\right)\mathrm{e}^{\left(((n+1/2)\pi/X)^2 D + k\right)t}}. \end{aligned} \tag{16}$$

For the adsorbed species on the surface with dry Ar feed, only the $H_{\mathrm{ads2}} \rightarrow H^+ + e^-$ reaction occurs on the surface of the cathode. Here, k_1 represents the reaction rate constant of $H_{\mathrm{ads2}} \rightarrow H^+ + e^-$, and β_{H} is the amount of adsorbed H atoms.

$$\begin{cases} \frac{\mathrm{d}\theta_{\mathrm{H}}}{\mathrm{d}t} = -k_1\beta_{\mathrm{H}} \\ \beta_{\mathrm{H}} = A_{\mathrm{H}}\mathrm{e}^{-k_1 t} \end{cases}. \tag{17}$$

When using a dry N_2 feed, if the NRR is mainly in accordance with the associative mechanism, $N_2H_{\mathrm{ads2}} \rightarrow N_{2\mathrm{ads2}} + H_{\mathrm{ads2}}$ and $H_{\mathrm{ads2}} \rightarrow H^+ + e^-$ are the reactions that occur on the surface of the cathode. Otherwise, $NH_{\mathrm{ads2}} \rightarrow N_{\mathrm{ads2}} + H_{\mathrm{ads2}}$ and $H_{\mathrm{ads2}} \rightarrow H^+ + e^-$ reactions occur. Here, k_2 represents the reaction rate constant of NH or N_2H decomposition, and $\beta_{\mathrm{NH\ or\ N2H}}$ is the amount of NH or N_2H adsorbed.

$$\begin{cases} \frac{\mathrm{d}\beta_{\mathrm{H}}}{\mathrm{d}t} = -k_1\beta_{\mathrm{H}} + k_2\beta_{\mathrm{N_2H\ or\ NH}} \\ \frac{\mathrm{d}\beta_{\mathrm{N_2H\ or\ NH}}}{\mathrm{d}t} = -k_2\beta_{\mathrm{N_2H\ or\ NH}} \\ \beta_{\mathrm{H}} = B_{\mathrm{H}}\mathrm{e}^{-k_1 t} + C_2\mathrm{e}^{-k_2 t} \end{cases}, \tag{18}$$

 © 2021 The Author(s). Published by the Royal Society of Chemistry

Open Access Article. Published on 07 January 2021. Downloaded on 11/11/2025 6:26:01 PM.
This article is licensed under a Creative Commons Attribution-NonCommercial 3.0 Unported Licence.

$$k_1\beta_H = k_1 B_H e^{-k_1 t} + \frac{k_1 k_2}{k_1 + k_2} B_H e^{-k_2 t}. \quad (19)$$

The third i_{ocv} reaction, which is due to discharge of the capacitor by the electrical double layer, is given as:

$$i_3 = A_C e^{-\frac{1}{RC}t}. \quad (20)$$

Therefore, the total i_{ocv} in a dry Ar feed and dry N_2 feed is given by:

$$i_{ocv} = \frac{\pi F D}{X^2}\sum_n (2n+1) \times \frac{(-1)^n \sqrt{k/D}\left(Ae^{\sqrt{k/D}X} - Be^{-\sqrt{k/D}X}\right) + \left(n+\frac{1}{2}\right)\frac{\pi}{X}(A+B)}{\left(\frac{k}{D} + \left(\left(n+\frac{1}{2}\right)\frac{\pi}{X}\right)^2\right) e^{(((n+1/2)\pi/X)^2 D + k)t}} + F A_H e^{-k_1 t} + A_C e^{-\frac{1}{RC}t}, \quad (21)$$

$$i_{ocv} = \frac{\pi F D}{X^2}\sum_n (2n+1) \times \frac{(-1)^n \sqrt{k/D}\left(Ae^{\sqrt{k/D}X} - Be^{-\sqrt{k/D}X}\right) + \left(n+\frac{1}{2}\right)\frac{\pi}{X}(A+B)}{\left(\frac{k}{D} + \left(\left(n+\frac{1}{2}\right)\frac{\pi}{X}\right)^2\right) e^{(((n+1/2)\pi/X)^2 D + k)t}} + F\left(k_1 B_H e^{-k_1 t} + \frac{k_1 k_2}{k_1 + k_2} B_H e^{-k_2 t}\right) + A_C e^{-\frac{1}{RC}t}. \quad (22)$$

The raw i_{ocv} to t_{ocv} data, collected at −0.2 V, −0.5 V, −1.5 V, and −1.9 V, were fitted using eqn (21) with the D, k, k_1, A_H, $(A + B)$, and $Ae^{\sqrt{k/D}X} - Be^{-\sqrt{k/D}X}$ parameters. Based on our assumptions, the D and k parameters do not depend on the applied voltage E; however, k_1, A_H, A, and B does. Values for all the parameters were determined for each E, and it was verified that the values of D and k do not depend on E, where D is 1.0×10^{-9} m^2 s^{-1} and k is 4.5×10^{-2} s^{-1}. With the D, k, A_H, and k_1 values obtained for the condition where a dry Ar gas atmosphere was used at the cathode side, the relationship between i_{ocv} and t_{ocv} under the same gas atmosphere under electrolysis conditions is provided by eqn (22). The raw i_{ocv} to t_{ocv} data, collected at −0.2 V, −0.5 V, −1.5 V, and −1.9 V, were fitted with the k_2, $(A + B)$, $Ae^{\sqrt{k/D}X} - Be^{-\sqrt{k/D}X}$, C_1, and C_2 parameters. Fig. 9 shows the fitting results for the current response at the cathode side under a dry Ar gas atmosphere at the voltages applied (−0.2 V, −0.5 V, −1.5 V, and −1.9 V). In this figure, "surface" denotes the current response by the decomposition of intermediates on the surface of the catalyst, "diffusion" denotes the response by the diffusion of H in the catalyst, "capacitor" denotes the response by the electrical double layer, and "fitted" represents the summation of these three contributions. Fig. 10 summarises the fitting results at the cathode side under a dry N_2 gas atmosphere at −0.2 V, −0.5 V, −1.5 V, and −1.9 V. The fitting results presented in Fig. 9 and 10 demonstrate that the developed model fits well with the experimentally measured current responses, and that the current responses assigned to the decomposition of the intermediates, diffusion of H atoms in the catalyst, and the electrical double layer are all positive and thus rational.

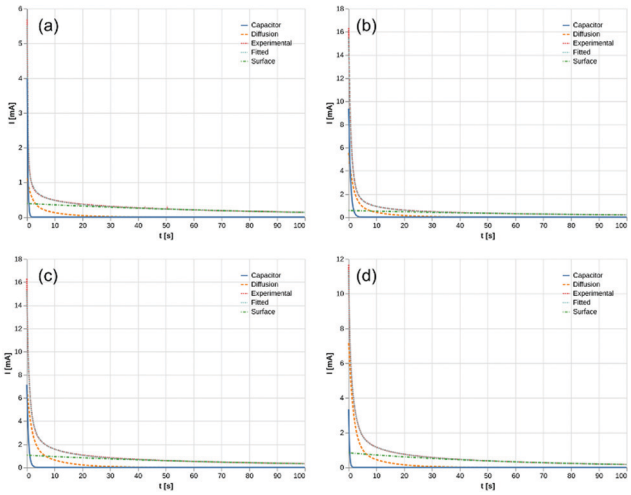

Fig. 9 Fitting results under dry Ar gas atmosphere at cathode side. (a) −0.2 V, (b) −0.5 V, (c) −1.5 V, and (d) −1.9 V. Surface: decomposition of intermediates on the surface of catalyst. Diffusion: diffusion of H in catalyst. Capacitor: electrical double layer.

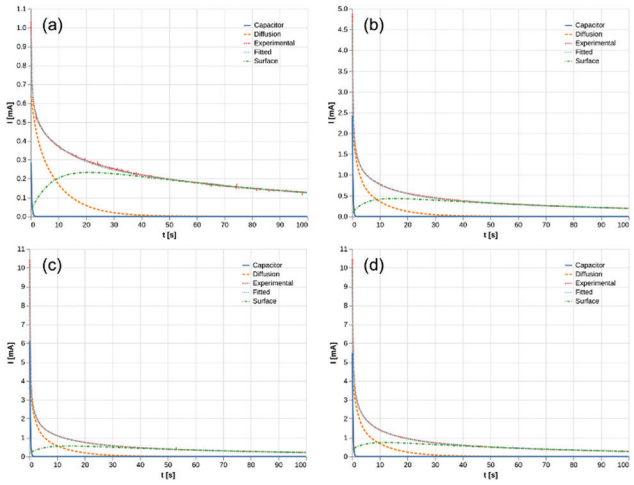

Fig. 10 Fitting results under dry N_2 gas atmosphere at cathode side. (a) −0.2 V, (b) −0.5 V, (c) −1.5 V, and (d) −1.9 V.

Table 1 Fitting results under dry Ar gas atmosphere at the cathode side

E [V]	k_1 [10^{-2} s^{-1}]	β_H [10^{-7} mol]	$1/(RC)$ [s^{-1}]
−0.2	1.0	3.9	3.9
−0.5	1.1	5.4	1.5
−1.5	1.2	9.2	1.8
−1.9	1.6	5.4	3.7

Open Access Article. Published on 07 January 2021. Downloaded on 11/11/2025 6:26:01 PM.
This article is licensed under a Creative Commons Attribution-NonCommercial 3.0 Unported Licence.

Table 2 Fitting results under dry N_2 gas atmosphere at the cathode side

E [V]	k_1 [10^{-2} s^{-1}]	k_2 [10^{-1} s^{-1}]	β_H [10^{-7} mol]	$\beta_{NH\ or\ N_2H}$ [10^{-7} mol]	$\beta_{NH\ or\ N_2H}/(\beta_{NH\ or\ N_2H} + \beta_H)$	$1/(RC)$ [s^{-1}]
−0.2	0.86	1.3	0.35	3.0	0.90	4.1
−0.4	1.0	1.8	0.39	4.0	0.91	4.8
−0.5	1.0	1.9	0.89	4.3	0.83	5.0
−1.5	1.2	1.8	1.5	4.2	0.74	4.9
−1.9	1.2	2.0	3.1	4.3	0.58	4.6

Tables 1 and 2 summarise the parameters obtained from eqn (21) and (22). The common parameters, k and D, are equal to 0.045 s^{-1} and 1.0×10^{-9} m^2 s^{-1}, respectively. The value of k_1 for all the applied voltages is approximately 0.012 s^{-1}, which corresponds to the $H_{ads2} \rightarrow H^+ + e^-$ reaction. The values of k_2 at −0.5, −1.5, and −1.9 V are similar, while k_2 at −0.2 V is quite different. This suggests that the main adsorbed species are different depending on the applied voltages, and could explain why N_2H_4 was only detected at −0.2 V. From these results, it is inferred that at −0.2 V, the NRR proceeds mainly in accordance with the associative mechanism, while at higher voltages, the dissociative mechanism dominates. The value of k_2 at −0.2 V is lower than that at −0.5, −1.5, and −1.9 V, which indicates that the energy barrier for the conversion of N_2* to N_2H* is lower than that for the conversion of N* to NH*. From Table 2, it is observed that the amounts of adsorbed NH* at −0.5, −1.5, and −1.9 V are similar, which could be equal to the total number of activation sites on the catalyst surface. The coverage of the activation sites by H atoms increased as the voltage increased; the high coverage could explain why the faradaic efficiency at −1.5 and −1.9 V is lower than that at −0.2 V and −0.5 V. The highest coverage ratio of NH* and the highest faradaic efficiency were achieved simultaneously at −0.4 V.

Conclusions

A novel Fe/BZY cathode catalyst was synthesised and applied with the addition of RuO_2 to the electrochemical synthesis of NH_3 using a proton-conducting electrolyte CsH_2PO_4/SiP_2O_7 at 220 °C and ambient pressure. With the addition of RuO_2, the NH_3 production rate increased and N_2H_4 was detected at −0.2 V; this might be because the oxidation of Fe was suppressed. The highest faradaic efficiency of 7.1% was achieved at −0.4 V (*vs.* OCV), which exhibited the highest NH_3 yield rate of 4.5×10^{-10} mol (s cm^2) at −1.5 V (*vs.* OCV). A by-product, N_2H_4, was detected at −0.2 V (*vs.* OCV). While the electrochemical NH_3 production rate using only Fe/BZY or RuO_2 was approximately 1.0×10^{-10} mol $(s\ cm^2)^{-1}$, which is comparable to the N_2 reduction rate over Fe/BZY–RuO_2, no N_2H_4 was detected. An equivalent circuit model was suggested to fit the impedance spectra. The fitting results were consistent with the highest faradaic efficiency achieved at −0.4 V. A model of the current response achieved by the potentiostatic pulse experiment was developed. The model comprised the decomposition of adsorbed intermediates on the surface of the cathode catalyst, diffusion of H in the cathode catalyst, and an electrical double layer. The current response was fitted to the model and the results showed that a high coverage ratio of NH* (and/or N_2H*) was attained at the applied voltage at which a high faradaic efficiency was achieved, and the coverage of NH* (and/or N_2H*) on mixed Fe/BZY–RuO_2 was much higher than that on only Fe/BZY or RuO_2 (Table 2 and Tables S4, S5, ESI†).

Conflicts of interest

The authors declare no conflicts of interest.

Acknowledgements

This work was supported by the Japan Society for the Promotion of Science (JSPS) KAKENHI grants 20H02521, Japan and Japan Science and Technology Agency (JST) CREST JPMJCR1441. Y. Y. was financially supported by the Graduate School of Engineering, The University of Tokyo Doctoral Student Special Incentives Program (SEUT). Y. Y. would like to thank Mr Naoya Fujiwara for his helpful comments and Mr Ryuichi Ohori for discussions regarding the model.

References

1 A. Jafari, A. Ebadi and S. Sahebdelfar, *React. Kinet., Mech. Catal.*, 2019, **126**, 307–325.
2 C. X. Guo, J. R. Ran, A. Vasileff and S.-Z. Qiao, *Energy Environ. Sci.*, 2018, **11**, 45–56.
3 Y. Bicer and I. Dincer, *Int. J. Energy Res.*, 2017, **41**, 1987–2000.
4 Y. Bicer and I. Dincer, *J. Electrochem. Soc.*, 2017, **164**, H5036–H5042.
5 S. Kishira, G. Qing, S. Suzu, R. Kikuchi, A. Takagaki and S. T. Oyama, *Int. J. Hydrogen Energy*, 2017, **42**, 26843–26854.
6 B. Ma, H. Zhao, T. S. Li, Q. Liu, Y. Luo, C. Li, S. Lu, A. M. Asiri, D. Ma and X. Sun, *Nano Res.*, 2020, 1–15.
7 C. J. M. van der Ham, M. T. M. Koper and D. G. H. Hetterscheid, *Chem. Soc. Rev.*, 2014, **43**, 5183–5191.
8 Y. Abghoui, A. L. Garden, J. G. Howalt, T. Vegge and E. Skúlason, *ACS Catal.*, 2016, **6**, 635–646.
9 L. Hu, A. Khaniya, J. Wang, G. Chen, W. E. Kaden and X. Feng, *ACS Catal.*, 2018, **8**, 9312–9319.
10 S. Licht, B. Cui, B. Wang, F.-F. Li, J. Lau and S. Liu, *Science*, 2014, **345**, 637–640.
11 M. Wang, S. Liu, T. Qian, J. Liu, J. Zhou, H. Ji, J. Xiong, J. Zhong and C. Yan, *Nat. Commun.*, 2019, **10**, 341.

 © 2021 The Author(s). Published by the Royal Society of Chemistry

Open Access Article. Published on 07 January 2021. Downloaded on 11/11/2025 6:26:01 PM.
This article is licensed under a Creative Commons Attribution-NonCommercial 3.0 Unported Licence.

12 X. Lv, F. Wang, J. Du, Q. Liu, Y. Luo, S. Lu, G. Chen, S. Gao, B. Zheng and X. Sun, *Sustainable Energy Fuels*, 2020, **4**, 4469–4472.
13 H. Yu, Z. Wang, D. Yang, X. Qian, Y. Xu, X. Li, H. Wang and L. Wang, *J. Mater. Chem. A*, 2019, **7**, 12526–12531.
14 D. Bao, Q. Zhang, F.-L. Meng, H.-X. Zhong, M.-M. Shi, Y. Zhang, J.-M. Yan, Q. Jiang and X.-B. Zhang, *Adv. Mater.*, 2017, **29**, 1604799.
15 T. Matsui, T. Kukino, R. Kikuchi and K. Eguchi, *J. Electrochem. Soc.*, 2006, **153**, A1077.
16 N. Lazouski, Z. J. Schiffer, K. Williams and K. Manthiram, *Joule*, 2019, **3**, 1127–1139.
17 A. R. Singh, B. A. Rohr, M. J. Statt, J. A. Schwalbe, M. Cargnello and J. K. Nørskov, *ACS Catal.*, 2019, **9**, 8316–8324.
18 A. R. Singh, B. A. Rohr, J. A. Schwalbe, M. Cargnello, K. Chan, T. F. Jaramillo, I. Chorkendorff and J. K. Nørskov, *ACS Catal.*, 2017, **7**, 706–709.
19 Y. Yuan, R. Kikuchi, A. Takagaki and S. T. Oyama, *ECS Trans.*, 2017, **78**, 451–459.
20 T. P. Dirkse and N. A. Hampson, *Electrochim. Acta*, 1972, **17**, 1113–1119.
21 P. Delahay, S. Oka and H. Matsuda, *J. Am. Chem. Soc.*, 1960, **82**, 329–332.
22 G. W. Watt and J. D. Chrisp, *Anal. Chem.*, 1952, **24**, 2006–2008.
23 G. Qing, K. Sukegawa, R. Kikuchi, A. Takagaki and S. T. Oyama, *J. Appl. Electrochem.*, 2017, **47**, 803–814.
24 G. Munteanu, L. Ilieva and D. Andreeva, *Thermochim. Acta*, 1997, **291**, 171–177.
25 M. A. Shipman and M. D. Symes, *Catal. Today*, 2017, **286**, 57–68.
26 C.-H. Li, S.-H. Hu, K.-W. Tay and Y.-P. Fu, *Ceram. Int.*, 2012, **38**, 1557–1562.
27 J.-Y. Lee and S. M. Lee, *Surf. Coat. Technol.*, 1986, **28**, 301–314.
28 R. McKibben, R. M. Sharp, D. A. Harrington, B. G. Pound and G. A. Wright, *Acta Metall.*, 1987, **35**, 253–262.
29 B. G. Pound, G. A. Wright and R. M. Sharp, *Acta Metall.*, 1987, **35**, 263–270.